Effects of Alloying on the Chemistry of CO and H_2S on Fe Surfaces

D. E. Jiang†

Department of Chemistry & Biochemistry, Box 951569, University of California, Los Angeles, California 90095-1569

Emily A. Carter*

Department of Mechanical and Aerospace Engineering and Program in Applied and Computational Mathematics, Princeton University, Princeton, New Jersey 08544-5263

Received: May 20, 2005; In Final Form: August 12, 2005

Deleterious gases such as CO and H_2S can cause degradation of steel by reacting with the metal surface. Here we consider whether alloying the steel surface might be able to inhibit these damaging surface reactions by raising the barriers to molecular dissociation. We employ first-principles density functional theory techniques to investigate the elementary reaction pathways and barriers for CO and H_2S on FeAl and Fe_3Si surfaces and compare them with pure Fe surfaces (as a model for steel). We find that H_2S dissociates on iron surfaces much more easily than CO does. Although FeAl surfaces raise the barriers for H_2S dissociation, they significantly lower the barriers for CO dissociation. On the other hand, Fe_3Si surfaces raise the barriers for CO dissociation, but they are as vulnerable as Fe surfaces to H_2S dissociation. Our findings suggest that alloying iron with Al or Si is unlikely to simultaneously increase its resistance to the initial stages of chemical degradation by CO and H_2S.

1. Introduction

The deterioration of structural metals due to corrosion incurs great cost to the economy. Investigating the gas−metal chemistry involved will help characterize the problem and ultimately help design more corrosion-resistant structural materials. Among the deleterious gases for structural metals, carbon monoxide (CO) and hydrogen sulfide (H_2S) are among the most notorious. CO is the main culprit for two high-temperature steel corrosion phenomena: carburization and metal dusting.[1,2] Both processes start with CO adsorption and dissociation on steel surfaces, followed by C ingress into the steel lattice. Carburization happens at a relatively high temperature (>800 °C) with the formation of internal carbides, which are brittle and can cause cracks in the steel substrate. Metal dusting is generally observed between 350 and 900 °C with a relatively high C activity, which shifts the chemical equilibrium toward graphite formation. Although metal dusting is preceded by carbide formation, those carbides are not stable and decompose to fine metal particles and graphite (or other forms of carbon).[3] Formation of surface layers of cementite, Fe_3C, with its lower melting point (compared to steel) may also result in melting of the steel surface. Those metal particles or molten cementite can easily be washed away by the gas stream, causing erosion of steel.

Gases containing H_2S attack structural metals such as iron aggressively. Due to favorable bulk thermodynamics and the relatively weak H−S bond, the barriers for H_2S dissociation on transition-metal surfaces are usually very small.[4−6] This leads to fast sulfur deposition on metal surfaces and subsequent sulfide formation. Sulfur can also cause the embrittlement of transition metals such as Ni and Fe.[7] Moreover, since H_2S deposits its hydrogen atoms on transition-metal surfaces, those hydrogen atoms can also embrittle metals such as Fe.[8,9]

In some special cases of metal erosion/corrosion, both CO and H_2S are present in the gas phase, e.g., in the propellant gases from a gun firing.[10] In the making of gun barrels, electroplated Cr is used to protect the steel substrate. However, the electroplating process produces Cr coatings that have microcracks. These microcracks grow and propagate to the substrate metal during operation, allowing those deleterious gases to travel along those cracks, subsequently attacking the substrate. Both iron sulfide and iron carbide are observed as erosion products.[10] Here we explore the possibility of designing an alternative thin film coating for steel with various ferrous intermetallic compounds. To survive harsh conditions, the intermetallic compound should be stable from room temperature to a relatively high temperature (e.g., 1300 °C), and the alloying element should not be a known embrittler of steel. Moreover, this element should not be so prone to reaction with CO or S-containing molecules. This element optimally would form a protective oxide scale when the ferrous intermetallic compound is exposed to air. From these considerations, we arrived at two candidate compounds to investigate: FeAl and Fe_3Si.

Industrial demand for lightweight structural materials for high-temperature applications has driven the interest in the research and development of intermetallic compounds.[11] FeAl- and Fe_3Si-based alloys have been shown to possess good corrosion resistance against carburization and sulfidation.[12−14] This resistance is thought to originate from the thin oxide scale formed on the alloy surfaces. We consider here the possible use of FeAl or Fe_3Si as a thin film coating on steel. Then, an oxide scale of alumina or silica may be able to protect the alloy coating in oxidizing environments. However, in some industrial applications, the gas environment is reducing in nature, and the oxide scale may either be destroyed or not form at all. Moreover, cracks in the oxide scale can also lead to gas attack of the base

* Corresponding author. Phone: +1-609-258-5391. Fax: +1-609-258-5877. E-mail: eac@princeton.edu.

† Present address. Oak Ridge National Lab, P.O. Box 2008 MS6367, Oak Ridge, TN 37831-6367.

10.1021/jp052656q CCC: $30.25
Published on Web 10/07/2005

alloy. In this work, we will address how the alloy surfaces will respond to the presence of both CO and H_2S under such conditions.

Although molecular adsorption and subsequent surface chemistry are well studied for elemental metal surfaces, chemistry on intermetallic surfaces is less well explored. With first-principles density functional theory (DFT) techniques, we have studied the adsorption and dissociation of CO and H_2S on pure Fe surfaces.[15−17] In the present work, we compare those findings with the chemistry of CO and H_2S on the Fe-alloy surfaces formed from the Fe intermetallic compounds FeAl and Fe_3Si. We first identify the site preference for CO, HS, H_2S, and their constituent atoms on low-index surfaces of Fe_3Si and FeAl. We then characterize pathways for dissociation of these molecules, including activation barriers, and compare them with those on pure Fe surfaces.

The paper is organized as follows. In section 2, we outline the calculational details. Results for the bulk and surface properties of FeAl and Fe_3Si are presented in section 3.1. We then show the results for adsorption in section 3.2 and dissociation in section 3.3. The surface chemistry and effects of alloying are discussed in section 3.4. We summarize and conclude in section 4.

2. Calculational Details

We perform first-principles calculations based on density functional theory (DFT).[18,19] The Vienna Ab Initio Simulation Package (VASP)[20,21] is used to solve the Kohn−Sham equations with periodic boundary conditions and a plane-wave basis set. Here we employ Blöchl's all-electron projector augmented wave (PAW) method,[22] as implemented by Kresse and Joubert,[23] within the frozen core approximation. We use the generalized gradient approximation (GGA) of PBE for the treatment of electron exchange and correlation.[24] Spin-polarized calculations are employed for Fe and Fe_3Si systems (bulk and surface), while nonspin-polarized ones are employed for FeAl systems, as explained further in section 3.1.

We use a kinetic energy cutoff of 400 eV for all the calculations, which converges the total energy to ∼1 meV/atom for the primitive unit cells of bulk Fe, FeAl, and Fe_3Si. The Monkhorst−Pack scheme[25] is used for the *k*-point sampling. The first-order Methfessel−Paxton method[26] is used for the Fermi surface smearing, with a width of 0.1 eV in order to obtain accurate forces. An equilibrium lattice constant of 2.834 Å is used for ferromagnetic bcc Fe, as we obtained earlier with a converged *k*-mesh of 15 × 15 × 15.[27] This lattice constant agrees well with the experimental value of 2.86 Å.[28] Bulk and surface properties for FeAl and Fe_3Si are shown and discussed in section 3.1.

To model gaseous CO, H_2S, HS, and C, O, H, and S atoms, we place a molecule or atom in a 10-Å cubic box. We perform a nonspin-polarized calculation for CO and H_2S, but spin-polarized calculations for open-shell C, O, HS, H, and S, where the valence electron configuration used for C, O, and S atoms is approximately the ^3P ground state (spin-polarized DFT "wave functions" are slightly spin-contaminated). Good agreement with experiment is achieved for molecular geometries, vibrational frequencies, and bond dissociation energies.[15,16]

We employ a five-layer slab with a 12-Å thick vacuum layer between periodic images to model all the surfaces and put adsorbates on one side of the slab; this produces a small dipole due to the dipole of the molecular adsorbate itself and to charge transfer between the adsorbate and the metal surface. However, we did not bother with a dipole correction to the total energy since it is generally small (<0.05 eV/cell). Only the top two layers of the five substrate layers are allowed to relax, together with the adsorbate layer. The bottom three layers are kept fixed in bulk positions to represent the semi-infinite bulk crystal beneath the surface. Allowing the middle layer of the substrate to relax only changes the total energy of the slab by ∼5 meV. When the maximum force acting on each of the relaxed atoms drops below 0.01 eV/Å, the structural relaxation is stopped. In this work, we study the surface chemistry of CO and H_2S in the low coverage regime (θ = 0.125−0.25 ML). We use a *k*-mesh for a surface cell that yields a *k*-point spacing of ∼0.03 (2π/Å) or smaller and that converges the adsorption energy to within 0.02 eV/adsorbate.

The Climbing Image Nudged Elastic Band (CI-NEB) method[29,30] is used to locate minimum energy paths (MEPs) and transition states. An interpolated chain of configurations (images) between the initial and final positions are connected by springs and relaxed simultaneously to the MEP. With the climbing image scheme, the highest-energy image climbs uphill to the saddle point. We use the same force tolerance for the transition-state search as used for structural relaxations. Typically, we first use the normal NEB method for ∼10 iterations (ionic steps) to roughly converge the MEP; then we switch on the climbing-image algorithm. After ∼50 more iterations, we can converge both the MEP and TS to the preset force tolerance.

Vibrational frequencies of adsorbates on surfaces are determined by diagonalizing a finite difference construction of the Hessian matrix with displacements of 0.02 Å (only allowing adsorbate atoms to move). The natures of the relaxed adsorbate configurations and the saddle points found by the CI-NEB method are characterized by vibrational frequency analyses, where the presence of one imaginary frequency indicates a transition state has been found, while ≥2 imaginary frequencies indicates a higher-order saddle point. The absence of imaginary frequencies is associated with a true minimum on the potential energy surface.

We also use calculated frequencies at the adsorption minima and transition states to estimate the zero-point energies (ZPE) at those configurations. We found that including ZPE lowers reaction barriers by 0.08 eV or less. Similarly, the resulting changes to the adsorption energies due to ZPE are found to be <+0.08 eV (per CO or H_2S). Since these changes are relatively small compared to other errors in the calculations and do not affect the general conclusions from the present work, we do not report ZPE corrections to the energetics.

3. Results and Discussion

3.1. Bulk and Surface Properties of FeAl and Fe_3Si. The ground state of bulk Fe is the body-centered-cubic (bcc) ferromagnetic (FM) phase. In our earlier work, we explored the various phases of Fe with PAW-DFT-GGA and compared the results with experiment.[27] Good agreement is obtained for the lattice parameter, local magnetic moment, and bulk modulus of bcc FM Fe. The structures of FeAl and Fe_3Si are related to bcc Fe. We present their structural properties next.

3.1.1. Bulk FeAl and Fe_3Si. FeAl has a CsCl (B2) type of structure, that is, one Al atom replacing Fe at the cubic center of bcc Fe (see Figure 1). Although magnetic susceptibility, Mössbauer, and nuclear magnetic resonance measurements indicate that perfectly ordered, stoichiometric FeAl is nonmagnetic in nature,[31,32] an FM ground state is found by DFT (both LDA and GGA) with a local magnetic moment of ∼0.7 μ_B for Fe.[33] This FM state is only slightly lower in energy (7 meV/atom) than the nonmagnetic (NM) state. Since the FM and NM

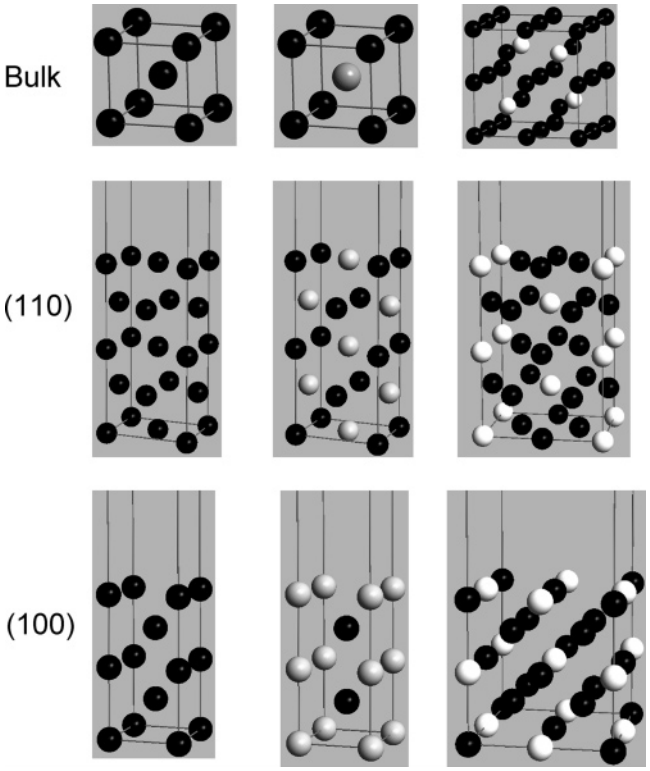

Figure 1. Bulk and surface structures of Fe, FeAl, and Fe_3Si. Fe atoms are in black, Al in gray, and Si in white.

TABLE 1: Comparison of DFT Predictions with Experiment for Bulk Properties of Fe_3Si: Lattice Parameter (*a*), Bulk Modulus (*B*), and Local Magnetic Moments (*M*)

	a (Å)	*B* (GPa)	M_{Fe-B} (μ_B)	M_{Fe-A} (μ_B)	M_{Si} (μ_B)
PAW-DFT-GGA-PBE	5.61	194	2.53	1.31	−0.05
experiment	5.65[a]	187[b]	2.2−2.4[c]	1.35[c]	−0.07[c]

[a] Ref 38. [b] Ref 39. [c] Ref 37.

states are almost degenerate and there are still controversies regarding the true ground state of FeAl,[34,35] we choose the NM state to model bulk FeAl and surfaces for simplicity. We obtain an FeAl equilibrium lattice constant of 2.87 Å, which agrees well with previous all-electron FLAPW-DFT-LDA calculations (2.87 Å) and experiment (2.91 Å), and an FeAl bulk modulus of 172 GPa, which improves upon the FLAPW-DFT-LDA result (200 GPa) compared with experiment (152 GPa).[36] The improved bulk modulus is no doubt due to the use of the GGA for exchange and correlation. These results for bulk FeAl suggest that PAW-DFT-GGA should provide a fair description of FeAl surfaces.

Bulk Fe_3Si has a DO_3-type of structure. It can be visualized as a (2 × 2 × 2) supercell of bcc Fe with four (out of eight) body-center Fe atoms replaced by Si. Those four Si atoms form a tetrahedron (Figure 1). We see that there are two types (A and B) of Fe atoms in the bulk Fe_3Si structure: the A-type is surrounded by four Fe atoms and four Si atoms in the first coordination shell, while the B-type is surrounded by eight nearest-neighbor Fe atoms. Magnetic susceptibility measurements show that Fe_3Si is FM.[37] We compare our results for bulk Fe_3Si with experiment[37−39] in Table 1 for the lattice parameter, bulk modulus, and local magnetic moments. The agreement is quite good, suggesting that since PAW-DFT-GGA describes bulk Fe_3Si well, the surfaces of Fe_3Si may also be reasonably well-described by this level of theory.

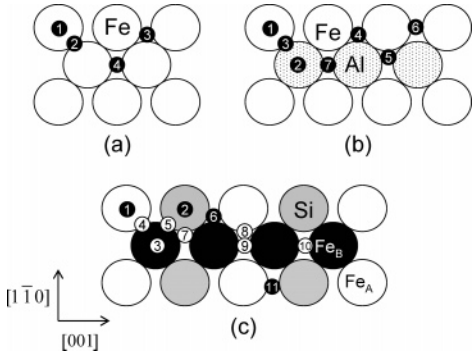

Figure 2. High-symmetry adsorption sites on (a) Fe(110): 1 = OT, 2 = SB, 3 = TF, and 4 = LB; (b) FeAl(110): 1 = OT-Fe, 2 = OT-Al, 3 = SB, 4 = TF-2Fe, 5 = TF-2Al, 6 = LB-2Fe, and 7 = LB-2Al; (c) Fe_3Si(110): 1 = OT-FeA, 2 = OT-Si, 3 = OT-FeB, 4 = SB-2Fe, 5 = SB−FeSi, 6 = TF−FeSi, 7 = TF-2Fe, 8 = TF-3Fe, 9 = LB-4Fe, 10 = LB-2Fe, and 11 = LB-FeSi. (Large circles are surface atoms, and small ones indicate adsorption sites. For Fe_3Si, the A-type Fe is denoted as a white circle and the B-type as a black circle. OT = on-top, SB = short-bridge, LB = long-bridge, and TF = 3-fold.)

3.1.2. FeAl and Fe_3Si Surfaces. We consider low Miller-index surfaces, since they are the most likely to be exposed. Because FeAl and Fe_3Si both belong to the bcc framework, (110) will be the closest-packed surface. The surface energy of Fe(100) is predicted by DFT-GGA to be only slightly higher than Fe(110),[40] so we also consider (100) surfaces for FeAl and Fe_3Si. Figure 1 displays bulk-terminated (110) and (100) surfaces for Fe, FeAl, and Fe_3Si. Although recent surface science studies (with low-energy electron diffraction and Auger electron spectroscopy) show that Al and Si tend to segregate on Fe−intermetallic surfaces after annealing,[41−48] our work focused on the bulk-terminated surfaces for simplicity. We note that some bulk-terminated surfaces are indeed obtained experimentally under certain conditions for FeAl and Fe_3Si. For example, bulk-terminated FeAl(110) can be obtained by annealing the surface at 400 °C,[49] while bulk-terminated FeAl(100) with Al at the surface can be obtained by annealing at 927 °C.[45] We therefore use the Al-terminated FeAl(100) in our work. This surface is expected to have a lower surface energy than the Fe-terminated structure, consistent with the lower surface energy of pure Al compared to pure Fe. For Fe_3Si(100), in principle the surface could be terminated with either 100% Fe atoms or 50% Fe and 50% Si. Because experiment shows that Si tends to segregate to the surface,[47] we investigate here the 50:50 terminated surface of Fe_3Si(100), as shown in Figure 1. FeAl(110) and Fe_3Si(110) each have only one bulk-terminated structure, which are also shown in Figure 1.

With DFT-GGA-PBE, we explored the structural relaxation of bulk-terminated FeAl and Fe_3Si surfaces. We find that the spacing between the surface Al layer and subsurface Fe layer of FeAl(100) contracts by 13.7%, in good agreement with experiment (14.6%).[50] We also find a slight buckling (∼0.1 Å) in the surface layers of FeAl(110), Fe_3Si(110), and Fe_3Si(100).

3.2. Adsorption Geometries and Energetics. High-symmetry adsorption sites on the (110) and (100) alloy surfaces are shown in Figures 2 and 3, respectively. From Fe(110) to FeAl(110) to Fe_3Si(110), the number of distinct sites increases; we identified 11 sites on Fe_3Si(110) to explore.

3.2.1. Adsorption on (110) Surfaces. Table 2 displays the most stable sites and the adsorption energies for all adsorbates considered on all three (110) surfaces. We predict that all open-shell species bind strongly (due to covalent bonding), while closed-shell species are less strongly bound (due to weaker donor/acceptor bonding) to these surfaces. We see that the C

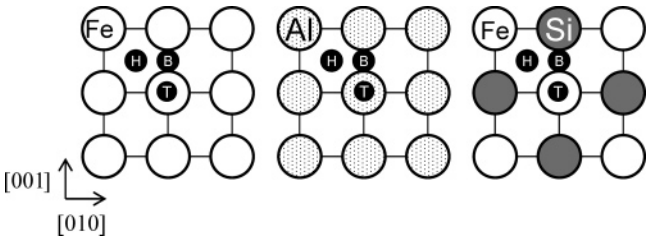

Figure 3. High-symmetry adsorption sites on Fe(100), FeAl(100), and $Fe_3Si(100)$: 4-fold hollow (H), 2-fold bridge (B), and 1-fold on-top (T) site. For $Fe_3Si(100)$, the on-top sites are divided into two types: 1-fold-Fe and 1-fold-Si.

TABLE 2: Most Stable Adsorption Sites and Energies (in eV; $E_{ad} = E_{A/Metal-slab} - E_{Metal-slab} - E_A$) of C, O, CO, H, S, HS, and H_2S on Fe(110), FeAl(110), and $Fe_3Si(110)$[a]

species	properties	Fe(110)	FeAl(110)	$Fe_3Si(110)$
C	site	LB	LB-2Fe	LB-4Fe
	E_{ad}	−7.8	−8.2	−7.7
O	site	TF	TF-2Fe	LB-4Fe
	E_{ad}	−6.3	−6.5	−6.2
CO	site	OT	OT-Fe	LB-4Fe
	E_{ad}	−1.9	−2.5	−2.2
H	site	TF	TF-2Fe	TF-3Fe
	E_{ad}	−3.0	−3.1	−3.2
S	site	LB	LB-2Fe	LB-4Fe
	E_{ad}	−5.8	−5.8	−5.8
HS	site	LB	LB-2Fe	LB-4Fe
	E_{ad}	−3.5	−3.8	−3.6
H_2S	site	SB	LB-2Fe	LB-4Fe
	E_{ad}	−0.6	−1.2	−0.9

[a] Site definitions are given in Figure 2.

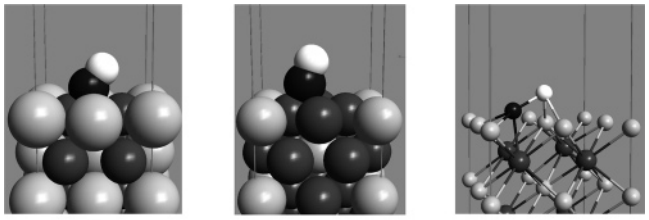

Figure 4. Tilted states of CO on alloy surfaces: (a) FeAl(110); (b) $Fe_3Si(110)$; (c) FeAl(100). Fe atoms in dark gray, C in black, and O in white, and Al and Si atoms in light gray.

atom binds strongly with all three surfaces and prefers high-coordination sites that maximize the number of Fe atoms. The site preference of S and HS on (110) surfaces is the same as that of C, only the binding is less strong than for C. O also binds strongly to (110) surfaces. As on Fe(110), O prefers the 3-fold (TF) site on FeAl(110), but it prefers the long-bridge-4Fe (LB-4Fe) site on $Fe_3Si(110)$. Indeed, the TF-3Fe site on $Fe_3Si(110)$ is not stable; the O atom relaxes to the LB-4Fe site when it is initially put at the TF-3Fe site. The H atom prefers the TF site that provides the maximum number of Fe atoms, and it binds strongly with all three (110) surfaces.

CO prefers the on-top (OT) site on Fe(110) in an upright fashion. This is also the case for CO on FeAl(110), where CO strongly adsorbs in a linear fashion on top of an Fe atom, while binding of CO to an Al site on FeAl(110) is ∼2 eV weaker. We also find a tilted state of CO on FeAl(110) that is ∼0.2 eV less stable than the upright OT configuration. We show this structure in Figure 4a, where we see that the C atom is displaced by ∼1.0 Å off the OT site along [001], and the molecular axis tilts off the surface normal (toward [001] by 35°). The CO stretching frequency is determined to be 1762 cm^{-1}. Interestingly, a similar tilted state of CO is also found on $Fe_3Si(110)$ (Figure 4b). Here the displacement off the OT site is 0.73 Å, the tilt angle is 25°, and the CO stretching frequency is 1900 cm^{-1}. Although CO prefers to reside in the LB-4Fe site in an upright fashion on $Fe_3Si(110)$, the tilted state is almost degenerate with the LB-4Fe site (within 0.02 eV/CO).

TABLE 3: Most Stable Adsorption Sites and Energies (in eV; $E_{ad} = E_{A/Metal-slab} - E_{Metal-slab} - E_A$) of C, O, CO, H, S, HS, and H_2S on Fe(100), FeAl(100), and $Fe_3Si(100)$[a]

species	properties	Fe(100)	FeAl(100)	$Fe_3Si(100)$
C	site	4-fold	4-fold	4-fold
	E_{ad}	−8.2	−6.8	−6.7
O	site	4-fold	2-fold	2-fold
	E_{ad}	−6.4	−6.5	−6.1
CO	site	4-fold-tilt	1-fold	1-fold-Fe
	E_{ad}	−2.1	−0.8	−1.2
H	site	4-fold	1-fold-Al	1-fold-Si
	E_{ad}	−2.7	−2.4	−2.6
S	site	4-fold	4-fold	2-fold
	E_{ad}	−6.0	−4.9	−4.5
HS	site	4-fold	2-fold	2-fold
	E_{ad}	−3.6	−3.3	−2.9
H_2S	site	2-fold	1-fold	1-fold-Fe
	E_{ad}	−0.5	−0.2	−0.5

[a] Site definitions are given in Figure 3.

The interaction between H_2S and metal surfaces is weakest among the adsorbates explored here, because H_2S does not have either unpaired electrons or low-lying empty π-orbitals. It can only interact with the surface via its lone pairs in a σ-donor mode. We see that H_2S also prefers binding to pure Fe sites, and it binds more strongly to FeAl(110) and $Fe_3Si(110)$ than to Fe(110). Electron density changes upon adsorption show that accumulation of electron density between the S atom in H_2S and its two nearest-neighbor Fe atoms increases with the concentration of alloying elements on (110) surfaces, namely, going from Fe(110) to $Fe_3Si(110)$ to FeAl(110). The charge rearrangement in each case involves simply a polarization of the electrons of H_2S. This trend of increased polarization as the alloying element concentration increases correlates well with the change in adsorption energy. Thus, alloying Fe appears to increase the extent of σ-donation by H_2S.

3.2.2. Adsorption on (100). FeAl(100) is terminated with Al, while $Fe_3Si(100)$ is terminated with half Fe atoms and half Si atoms, as shown in Figures 1 and 3. The Si atoms at the $Fe_3Si(100)$ surface exhibit a near-zero ($-0.07\ \mu_B$) local magnetic moment, as they do in the bulk, indicating that there are no dangling bonds associated with them. Table 3 displays the most stable sites and their adsorption energies on (100) surfaces. Once again, the open-shell species (atoms and SH) are much more strongly bound than the closed-shell molecules, due to the former's ability to form strong covalent bonds to the metal surface. We see that C always prefers a 4-fold site and adsorbs most strongly on Fe(100). The presence of Si on the $Fe_3Si(100)$ surface destabilizes C by ∼1.5 eV; likewise, C adsorption on the fully Al-terminated FeAl(100) surface is ∼1.4 eV less strongly bound than on a pure Fe(100) surface. This is to be contrasted with O adsorption on the three surfaces, where O binds with nearly equal affinity to all of them. This is likely due to the high affinity of Si or Al for O. Moreover, we see that O prefers the 2-fold bridge site on FeAl(100) and $Fe_3Si(100)$. Since FeAl(100) is terminated with an Al layer, it makes sense to compare it with Al(100). Extended appearance-potential fine structure analysis[51] shows that O prefers the 4-fold hollow site and sits slightly below the surface layer of Al(100). Recent DFT-embedded cluster calculations[52] confirm this site preference of O atoms on Al(100). The difference between Al(100) and

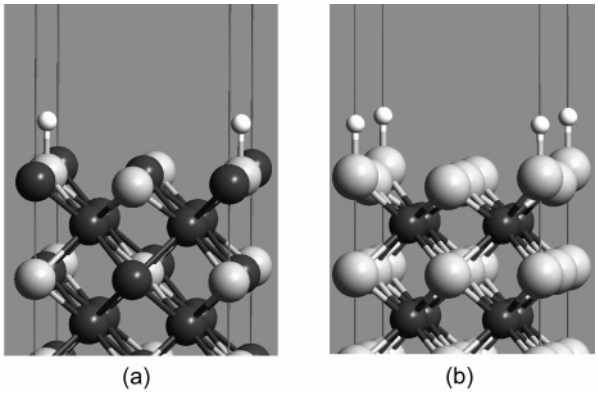

Figure 5. Most stable adsorption sites for H on (100): (a) Fe_3Si; (b) FeAl. Fe atoms in dark gray, H in white, and Al and Si atoms in light gray.

FeAl(100) for O adsorption is likely due to the fact that the interlayer spacing of Al(100) is much larger (by 0.6 Å) than that of FeAl(100). As a result, O atoms can burrow more easily into the surface layer at the hollow site, in preparation to go into the subsurface and to begin to form aluminum oxide. At the 2-fold site of $Fe_3Si(100)$, O interacts more with Si than Fe, as evidenced by bond lengths that are shorter (longer) than the sum of atomic radii for O−Si (O−Fe): $r_{O-Si} = 1.65$ Å and $r_{O-Fe} = 2.00$ Å, compared with $r_O + r_{Si} = 1.83$ Å and $r_O + r_{Fe} = 1.93$ Å.[53] Oxygen atoms tend to form covalent bonds with Si atoms, as in the bulk SiO_2, where an O atom bridges two Si atoms. As a result, it makes sense that O atoms move to a lower coordination 2-fold bridge site on $Fe_3Si(100)$, since O atoms prefer to bond more covalently to the Si atoms on the surface.

We find that H prefers the 4-fold hollow site on Fe(100),[54] in agreement with experiment.[55] The 2-fold bridge site is also a minimum for H, but the 1-fold OT site is a higher-order saddle point.[54] Unexpectedly, we find that H prefers the 1-fold site on FeAl(100) and also the 1-fold Si site of $Fe_3Si(100)$. This is in contrast with Al(100), where H prefers the 2-fold bridge site.[56] Figure 5 shows the two structures. It is rare for H to adsorb on the 1-fold site of a metallic surface with 4-fold symmetry.[57] This type of bonding indicates that the H−Al and H−Si interactions are likely very covalent in character, resembling, for example, the Si−H bonds on the Si(100) surface, despite the lack of dangling bond character on the bare $Fe_3Si(100)$ surface. The bond lengths for H−Al and H−Si are found to be 1.627 and 1.524 Å, respectively, which are similar to gaseous AlH ($r_{H-Al} = 1.648$ Å) and SiH_4 ($r_{H-Si} = 1.480$ Å),[58] lending credence to the idea that the bonding of H to FeAl(100) and $Fe_3Si(100)$ involves localized, covalent bonds. Site-projected, orbital-resolved local densities of states (LDOS) shown in Figure 6 also support this picture. H 1s states overlap strongly with Si 3s states around −9 eV and 3pz states between −6 and −4 eV for $H/Fe_3Si(100)$ (Figure 6a). On FeAl(100), H 1s states overlap with Al 3s between −7 and −4 eV and 3pz between −4 and −1 eV (Figure 6b). The corresponding metal−H antibonding states appear above the Fermi level, a clear signature of covalent bonding (as in the σ/σ^* levels in H_2).

CO adsorbs most strongly on Fe(100), preferring a 4-fold tilted configuration over the OT site by 0.6 eV at 0.25 ML. This site was identified previously by several different surface science techniques. A very low CO stretching frequency (1210 cm^{-1}) was observed[59] by high-resolution electron energy loss spectroscopy (HREELS). Our work also yields a very low frequency of 1189 cm^{-1}, consistent with experiment. For CO adsorption on FeAl(100), we also find a tilted state that is essentially degenerate (within 0.01 eV) with the OT site. At both sites, CO is weakly bound to the surface. This adsorption energy is in line with the experimental observation that CO physisorbs on Al(100) at low temperatures and desorbs at room temperature.[60] The tilted state of CO on FeAl(100) is found to have a dramatically lower CO stretching frequency (853 cm^{-1}) than on Fe(100), and the CO bond is very much elongated ($r_{C-O} = 1.475$ Å; $\theta_{tilt} = 61.2°$; see Figure 4c), suggesting that despite its weak adsorption energy, it is highly activated. This surprising finding can be understood as a balance between strong intrinsic adsorption and destabilization of the CO molecule by breaking its π-bonds.[61] On $Fe_3Si(100)$, CO prefers to adsorb on Fe with an upright, on-top fashion. Although the adsorption site for CO on $Fe_3Si(100)$ has not been established experimentally, photoemission spectra imply that CO is indeed upright on $Fe_3Si(100)$.[62] For comparison, we note HREELS and temperature-programmed desorption (TPD) results suggest[63,64] that CO adsorbs on-top of an Si atom in an upright fashion on Si(100), with an adsorption energy of −0.63 eV predicted by DFT with a hybrid exchange-correlation functional and a cluster model.[65] In our work, CO adsorbs on the Si atom of $Fe_3Si(100)$ with an energy of only −0.4 eV, much weaker than on the Fe atom, indicating that Si repels CO on $Fe_3Si(100)$.

S adsorbs most strongly on Fe(100), followed by FeAl(100), and then $Fe_3Si(100)$. While S prefers the high coordination sites on the metallic surfaces [Fe(100) and FeAl(100)], it switches to the 2-fold site on $Fe_3Si(100)$, as in the case for oxygen. Generally, then, the presence of Si on the Fe surface forces more covalent bonding to adsorbates. HS adsorption follows the same trend as S in terms of site preference and surface affinity, because the adsorption behavior of HS on (100) surfaces is also dictated by the unpaired electron on S. The binding energies

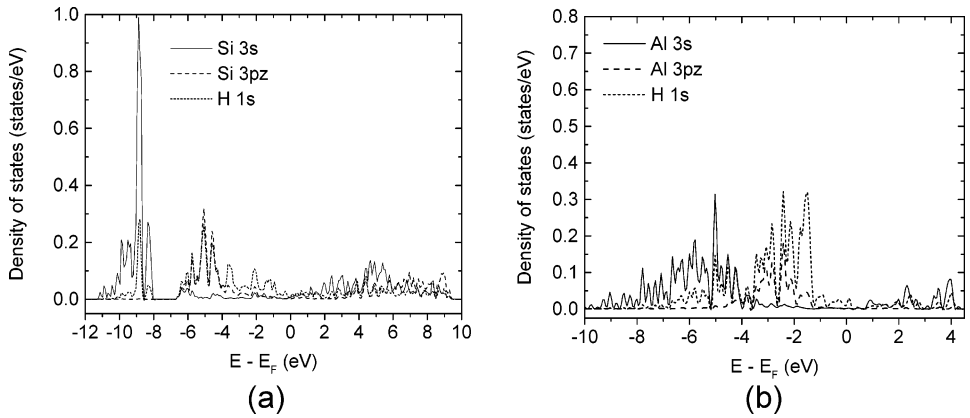

Figure 6. Site-projected, orbital-resolved LDOS for (a) the H adatom and the surface Si atom connected to the H atom from Figure 5a; and (b) the H adatom and the surface Al atoms connected to the H atom from Figure 5b.

TABLE 4: Dissociation Barriers for CO and H_2S on Fe, FeAl, and Fe_3Si

barriers (eV)	Fe(110)	Fe(100)	FeAl(110)	FeAl(100)	Fe_3Si(110)	Fe_3Si(100)
$CO \rightarrow C + O$	1.5	1.1	1.3	0.4	2.4	1.3
$H_2S \rightarrow H + HS$	0.1	0.3	0.4	0.3	0.1	0.2
$HS \rightarrow H + S$	0.	0.3	0.3	0.7	0.	0.4

between HS and (100) surfaces are >1.6 eV less strong than between S atoms and (100) surfaces, due to the fewer number of unpaired electrons in HS. Interestingly, HS is bonded linearly to the Fe(100) surface at the 4-fold hollow site, whereas HS is bent toward the surface on both FeAl(100) and Fe_3Si(100) at the 2-fold bridge site by 66.6° and 70.0°, respectively, indicating once again that alloying the surface enhances covalent bonding to adsorbed species.

H_2S adsorbs extremely weakly on all three surfaces, with the weakest interaction between H_2S and FeAl(100). On both FeAl(100) and Fe_3Si(100), the H_2S molecular plane is almost parallel to the surface. The difference is that the S atom of H_2S binds to Al on FeAl(100) but to Fe on Fe_3Si(100). This type of parallel on-top configuration is also found for H_2S on Fe(100), but its adsorption energy is predicted to be ~0.1 eV weaker than the 2-fold bridge site, where the molecular plane is oriented perpendicular to the surface.[15]

3.3. Dissociation Pathways and Transition States. After the preferred adsorption sites for CO, H_2S, HS, and atomic species were identified on the surfaces, we then located minimum energy paths and transition states for CO dissociation and H_2S dehydrogenation. Table 4 displays the barriers we obtained on the six surfaces for the three dissociation processes.

3.3.1. CO Dissociation. After examining all the structures at the transition state for CO dissociation, we find that they share the common feature that CO lies side-on at a bridge site, presumably due to the need to break the π-bonds of CO. This transition-state configuration has been predicted previously for CO and N_2 dissociation on metal surfaces.[66,67] We predicted that CO dissociation on Fe(110) has a barrier of 1.5 eV,[16] while we determined the barrier on Fe(100) to be 1.1 eV, which agrees very well with experiment (1.09 eV)[68] and previous DFT work.[69,70] The lower barrier on Fe(100) can be attributed to the highly tilted state of CO on Fe(100), which has a much weakened CO bond already before dissociation. The OT site preference by CO on Fe(110) then requires more rearrangement of the CO molecule to reach the TS, leading to a higher barrier.

The barrier for CO dissociation on FeAl is found to be lower than that for the corresponding pure Fe surface. This is especially true for FeAl(100). We predict a barrier of only 0.4 eV on FeAl(100), which is ~0.7 eV lower than on pure Fe(100). Figure 7 shows the minimum energy path (MEP). This dissociation pathway is the same as that on Fe(100). The lower barrier on FeAl(100) again can be attributed to the much weakened initial state, as we discussed above (Figure 4c). In this state, the CO bond length (1.475 Å) is even larger than that in gaseous methanol (H_3C-OH, 1.425 Å[58]), indicating that the C−O bond order in this site is reduced to ≤1. An interaction between C and the subsurface Fe atom, as well as the high affinity of O to surface Al atoms, lead to this highly tilted state. This is supported by the fact that we also found this tilted state of CO on just a monolayer of Al on Fe(100), and we demonstrated a significant interaction between subsurface Fe and C for this latter, analogous surface.[61] The smaller barriers on FeAl surfaces indicate that FeAl alloys may be even more susceptible to carburization than is Fe itself.

CO is found to have a higher dissociation barrier on Fe_3Si than on the corresponding pure Fe surface. For example, the CO dissociation barrier is 2.4 eV on Fe_3Si(110), 0.9 eV higher than on Fe(110). The structure of the MEP for breaking the CO bond on Fe_3Si(110) is found to be similar to what we predicted for CO dissociation on Fe(110).[16] Namely, CO first moves off the OT site, then tilts toward the surface, and dissociates over a bridge site. This pathway is also adopted by CO dissociation on Fe_3Si(100), where CO prefers upright on-top adsorption on the Fe atom. So CO dissociation on Fe_3Si(100) is quite different from that on Fe(100) or FeAl(100), where a side-on adsorption state leads to a smaller dissociation barrier. The increase in dissociation barrier (relative to pure Fe) on Fe_3Si(100) is smaller (~0.2 eV) than for Fe_3Si(110). However, since Fe_3Si(110) has a surface energy ~10% less than that of Fe_3Si(100), Fe_3Si(110) is more likely to be the preferred facet exposed. So overall Fe_3Si is expected to be more resistant to initial CO attack (i.e., adsorption and dissociation) than is pure Fe.

3.3.2. H_2S Dissociation. The closest-packed Fe(110) surface is found to be very efficient in dissociating H_2S. The first dehydrogenation step has a small barrier (0.1 eV), and the second step is barrierless.[17] On Fe(100), the barriers are slightly higher.[15] The MEPs show that the H−S bond breaks by bending the bond toward the surface and breaking off the H atom on top of an Fe atom.[15,17] From Table 4, we see that the barriers for the two dehydrogenation steps on Fe_3Si(110) are similar to those on Fe(110). The MEPs on those two surfaces are also found to be similar. Figure 8 shows the first dehydrogenation step on Fe_3Si(110): H_2S rotates in its molecular plane, bends one H−S bond toward the surface, and then breaks off one H atom on a nearby Fe atom. This mechanism is exactly the same as that on Fe(110).[17] The second dehydrogenation step to form S from SH also involves the same bond-breaking configuration for both pure Fe and Fe_3Si(110). If we look at the Fe_3Si(110) surface, we see that the Fe atoms on Fe_3Si(110) form a local environment that resembles Fe(110). The ensemble size required for reaction[71] here seems to be only 4 atoms of Fe. This similar environment leads to similar barriers and pathways for H_2S dehydrogenation.

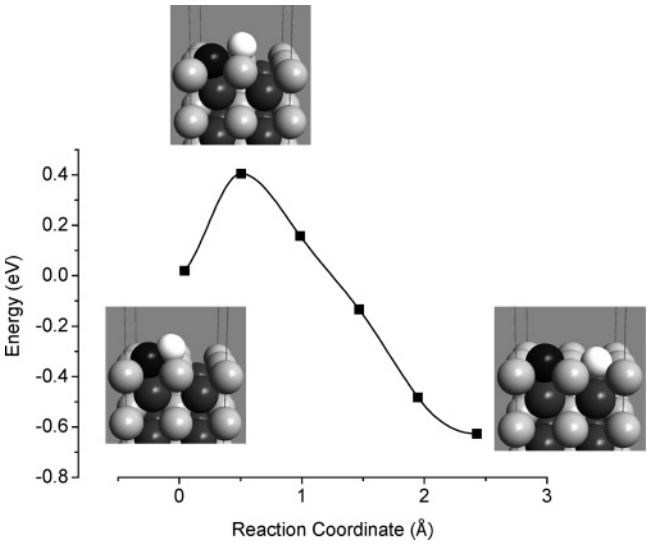

Figure 7. PAW-DFT-GGA minimum energy path for CO dissociation on FeAl(100) and the structures for the initial, transition state, and final states. Fe atoms are in dark gray, Al in light gray, O in white, and C in black.

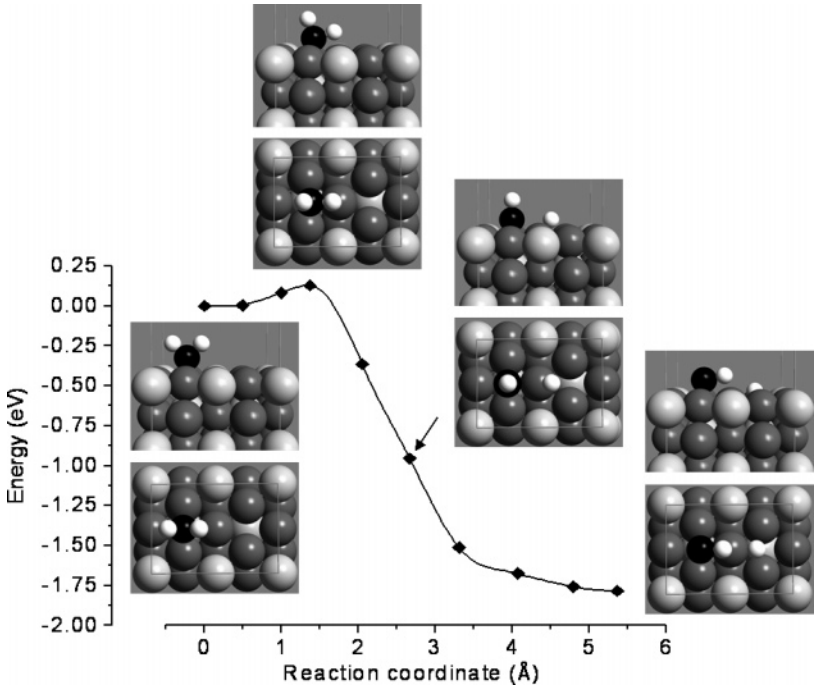

Figure 8. PAW-DFT-GGA minimum energy path for H_2S dissociation on $Fe_3Si(110)$ and several intermediate structures along the path (the upper images are side views, and bottom are top views). Fe atoms are in dark gray, Si in light gray, S in black, and H in white.

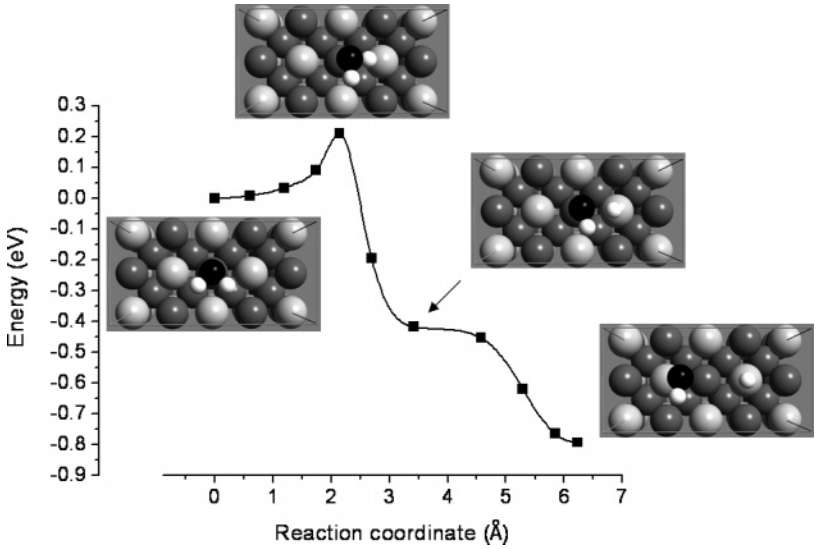

Figure 9. PAW-DFT-GGA minimum energy path for H_2S dissociation on $Fe_3Si(100)$ and several intermediate structures along the path. Fe atoms are in dark gray, Si in light gray, S in black, and H in white.

The surface of $Fe_3Si(100)$ is comprised of half Fe and half Si atoms, and their lateral sub-lattices interleave. This affects the H_2S dehydrogenation mechanism. Figure 9 shows the MEP for the first dehydrogenation step. We see that H_2S adsorbs parallel to the surface and on top of an Fe atom in the initial state. Then the H_2S molecule moves toward a nearby Si atom and points the H atom of one H−S bond to the Si atom at the transition state. The H atom then breaks off, moves on top of the Si atom, and stays there. The HS group moves back, passing on top of the Fe atom and then diffusing to the bridge site. This pathway is Si-mediated and thus very different from that on Fe(100), even though the barrier is not significantly different. After the first step, HS adsorbs asymmetrically at the bridge site, resulting in the H atom of the HS group being very close to a nearby Fe atom (Figure 9). So it is understandable that the second dehydrogenation step is found to be mediated by that Fe atom. Comparing Fe_3Si with pure Fe for H_2S dissociation, we see that Fe_3Si is unfortunately as susceptible as Fe to initial H_2S attack.

FeAl(100) is terminated with Al, and FeAl(110) does not have a local surface environment (reaction ensemble size) similar to Fe(110). So we expect different pathways for H_2S dissociation on FeAl surfaces. Figure 10 shows the MEPs for the first dehydrogenation step on FeAl(110) and on FeAl(100). Even though H_2S starts with a similar geometry on FeAl(110) as on Fe(110) and $Fe_3Si(110)$, the dissociation pathway is distinctly different. Unlike on Fe(110) or $Fe_3Si(110)$, where H_2S rotates in its molecular plane, instead H_2S bends out of the molecular plane toward the surface. However, as on Fe(110) or Fe_3Si-(110), where H_2S breaks off the first H atom on top of an Fe atom, H_2S also uses an Fe atom instead of Al to dissociate the H−S bond on FeAl(110). This is also the case for FeAl(100),

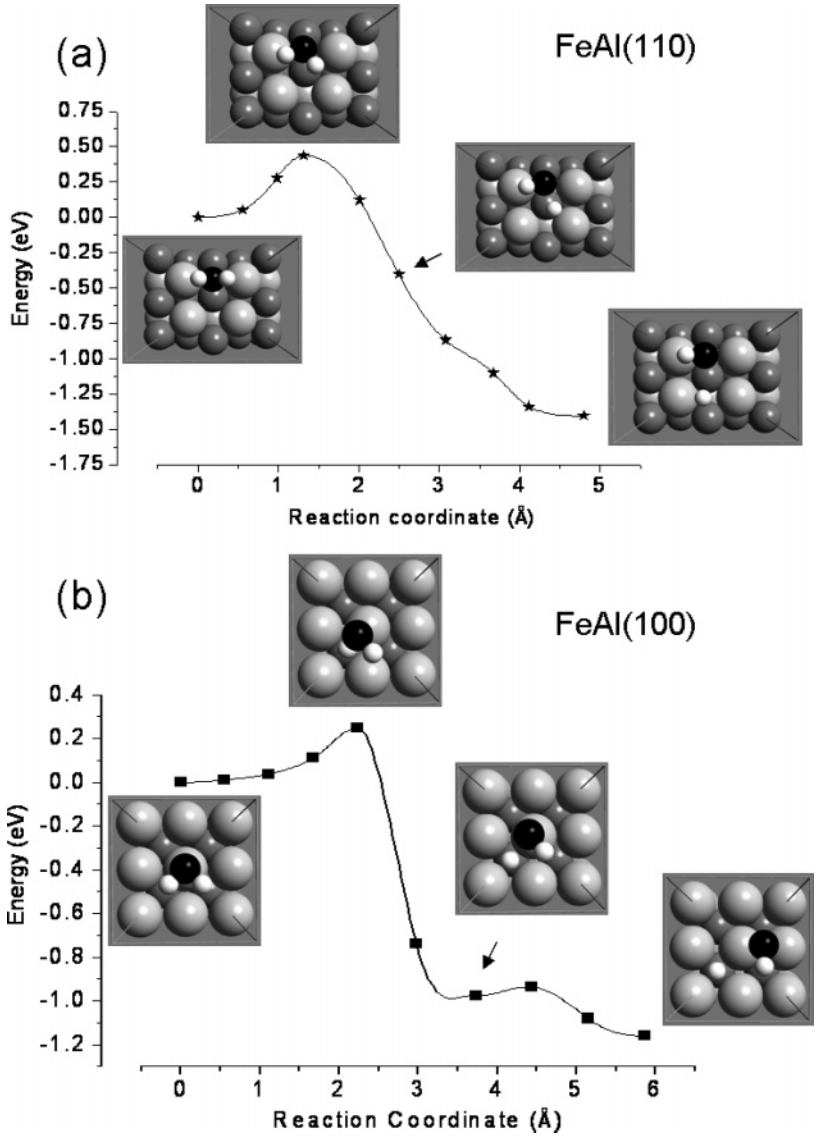

Figure 10. PAW-DFT-GGA minimum energy paths and several intermediate structures along the paths for H_2S dissociation on FeAl(110) (a) and FeAl(100) (b). Fe atoms are in dark gray, Al in light gray, S in black, and H in white.

where Fe is in the subsurface. In Figure 10b, we see that H_2S bends one of the H−S bonds toward a subsurface Fe atom, and the H−S bond breaks by transferring the H atom to the subsurface Fe atom. The second dehydrogenation step on FeAl(100) follows the same pathway as the first one, only with a barrier that is ∼0.4 eV higher. This indicates that the HS group may be a stable intermediate on FeAl(100) that could be observed experimentally.

3.4. Discussion of the CO and H_2S Surface Chemistry on Fe and Alloy Surfaces. From Table 4, we see that H_2S is a more aggressive attacker of iron, as shown by the very small dissociation barriers of H_2S on Fe. Interestingly, the closest-packed Fe(110) surface turns out to be more efficient than the more open Fe(100) surface in the dehydrogenation of H_2S. Since the initial deposition of sulfur is kinetically facile, the sulfidation process is probably controlled by other factors. Sulfidation of Fe films shows that the kinetics follows a parabolic curve, indicating the reaction is solid-state diffusion controlled (by Fe ions).[72,73] Accordingly, the bulk diffusion barrier is much higher than the H_2S dissociation barrier. Grabke and co-workers have observed that a small concentration of H_2S in a CO/H_2 gas mixture can retard the metal dusting process.[74,75] This is likely to be due to the facile deposition of S atoms that block the surface sites for CO adsorption and/or dissociation (i.e., S poisons the surface). Our prediction of strong bonding between Fe and S (∼6 eV) is consistent with this idea.

CO dissociation on Fe(100) is found to be ∼0.4 eV lower than on the closest-packed Fe(110) surface, indicating that more open surfaces will lead to smaller barriers for CO dissociation. So we expect that surface defects and steps on actual steel surfaces will enhance CO dissociation. This agrees with the observation that after argon ion sputtering, Fe(110) becomes more efficient in breaking the CO bond.[76]

The surfaces of the intermetallic compounds FeAl and Fe_3Si provide a way to investigate the effect of alloying on the Fe surface chemistry of CO and H_2S. Again, our goal was to explore if alloying could raise the barriers to molecular dissociation such that initial attack of steel surfaces could be inhibited through forming surface alloys. From Table 4, we see that use of FeAl surfaces increases the dehydrogenation barriers of H_2S up to 0.4 eV. Unfortunately, the CO dissociation barrier is smaller on FeAl surfaces, especially on FeAl(100) [0.7 eV lower than on Fe(100)]. On Fe_3Si surfaces, the trend is reversed. The resistance against initial CO attack is increased, but the small H_2S dissociation barriers are basically unchanged on Fe_3Si surfaces compared with Fe surfaces. Our work indicates that

Al is not a good choice for an alloying element in terms of preventing initial CO attack and that H_2S resistance is difficult to achieve by alloying. If carburization is the only concern, then adding Si to the steel surface could be helpful.

4. Summary and Conclusions

Using periodic density functional theory within the generalized-gradient approximation to electron exchange and correlation, we have studied CO and H_2S adsorption and dissociation on low-index Fe alloy surfaces. We have investigated chemistry on the (110) and (100) surfaces of Fe, FeAl, and Fe_3Si. We find that CO dissociates via a lying-down, bridging transition state on all (110) and (100) surfaces examined. H_2S dissociates via an on-top-of-Fe path on (110) surfaces. The similar local reaction ensemble size of Fe atoms on $Fe_3Si(110)$ compared to Fe(110) leads to analogous pathways and barriers for H_2S dissociation. Interestingly, subsurface Fe participates in CO and H_2S dissociation on FeAl(100). We found a precursor state of CO on FeAl(100) with an extremely low C−O stretching frequency and a low dissociation barrier. FeAl is predicted to be more resistant to initial H_2S attack, but more vulnerable to initial CO attack than Fe. Fe_3Si is predicted to be more resistant to initial CO attack than Fe, but as susceptible as Fe to initial H_2S attack. Neither Si nor Al alloying with Fe can simultaneously protect steel against the initial stages of chemical degradation by CO and H_2S. However, future investigations of the subsequent solid-state chemistry (diffusion and compound formation) to see if Al or Si could inhibit the subsequent degradation of steel would be worthwhile. If this next avenue also proves ineffective, an alternative approach to protecting steel is to develop coatings that can form protective oxide scales and that do not fracture easily. We are pursuing such ideas at present.

Acknowledgment. This work was supported by the Army Research Office. We thank the Maui High Performance Computing Center, the Army Research Laboratory Major Shared Resources Center, and the Naval Oceanographic Office Major Shared Resource Center for providing CPU time.

References and Notes

(1) Grabke, H. J. *Carburization: A High-Temperature Corrosion Phenomenon*; Materials Technology Institute: St. Louis, MO, 1998.
(2) Grabke, H. J.; Muller-Lorenz, E. M.; Schneider, A. *ISIJ Int.* **2001**, *41*, S1.
(3) Grabke, H. J.; Krajak, R.; Paz, J. C. N. *Corros. Sci.* **1993**, *35*, 1141.
(4) Hegde, R. I.; White, J. M. *J. Phys. Chem.* **1986**, *90*, 296.
(5) Huntley, D. R. *Surf. Sci.* **1990**, *240*, 13.
(6) Blyth, R. I. R.; Searle, C.; Tucker, N.; White, R. G.; Johal, T. K.; Thompson, J.; Barrett, S. D. *Phys. Rev. B* **2003**, *68*, 205404.
(7) Rice, J. R.; Wang, J. S. *Mater. Sci. Eng. A* **1989**, *107*, 23.
(8) Srikrishnan, V.; Liu, H. W.; Ficalora, P. J. *Scr. Metall.* **1975**, *9*, 1341.
(9) Briant, C. L.; Sieradzki, K. *Phys. Rev. Lett.* **1989**, *63*, 2156.
(10) Cote, P. J.; Rickard, C. *Wear* **2000**, *241*, 17.
(11) Sauthoff, G. *Intermetallics*; VCH: Weinheim, 1995.
(12) Kumar, K. S.; Liu, C. T. *JOM*—J. Miner. Met. Mater. Soc. **1993**, *45*, 28.
(13) George, E. P.; Yamaguchi, M.; Kumar, K. S.; Liu, C. T. *Annu. Rev. Mater. Sci.* **1994**, *24*, 409.
(14) Liu, C. T.; George, E. P.; Maziasz, P. J.; Schneibel, J. H. *Mater. Sci. Eng. A* **1998**, *258*, 84.
(15) Jiang, D. E.; Carter, E. A. *J. Phys. Chem. B* **2004**, *108*, 19140.
(16) Jiang, D. E.; Carter, E. A. *Surf. Sci.* **2004**, *570*, 167.
(17) Jiang, D. E.; Carter, E. A. *Surf. Sci.* **2005**, *583*, 60.
(18) Hohenberg, P.; Kohn, W. *Phys. Rev.* **1964**, *136*, B864.
(19) Kohn, W.; Sham, L. J. *Phys. Rev.* **1965**, *140*, A1133.
(20) Kresse, G.; Furthmüller, J. *Phys. Rev. B* **1996**, *54*, 11169.
(21) Kresse, G.; Furthmüller, J. *Comput. Mater. Sci.* **1996**, *6*, 15.
(22) Blöchl, P. E. *Phys. Rev. B* **1994**, *50*, 17953.
(23) Kresse, G.; Joubert, D. *Phys. Rev. B* **1999**, *59*, 1758.
(24) Perdew, J. P.; Burke, K.; Ernzerhof, M. *Phys. Rev. Lett.* **1996**, *77*, 3865.
(25) Monkhorst, H. J.; Pack, J. D. *Phys. Rev. B* **1976**, *13*, 5188.
(26) Methfessel, M.; Paxton, A. T. *Phys. Rev. B* **1989**, *40*, 3616.
(27) Jiang, D. E.; Carter, E. A. *Phys. Rev. B* **2003**, *67*, 214103.
(28) Acet, M.; Zähres, H.; Wassermann, E. F.; Pepperhoff, W. *Phys. Rev. B* **1994**, *49*, 6012.
(29) Jónsson, H.; Mills, G.; Jacobsen, K. W. Classical and Quantum Dynamics in Condensed Phase Simulations. In *Classical and Quantum Dynamics in Condensed Phase Simulations*; Berne, B. J., Ciccotti, G., Coker, D. F., Eds.; World Scientific: Singapore, 1998; p 385.
(30) Henkelman, G.; Uberuaga, B. P.; Jónsson, H. *J. Chem. Phys.* **2000**, *113*, 9901.
(31) Miyatani, K.; Iida, S. *J. Phys. Soc. Jpn.* **1968**, *25*, 1008.
(32) Frankel, R. B.; Sellmeye, D. J.; Blum, N. A. *Phys. Lett. A* **1970**, *A 33*, 13.
(33) Bogner, J.; Steiner, W.; Reissner, M.; Mohn, P.; Blaha, P.; Schwarz, K.; Krachler, R.; Ipser, H.; Sepiol, B. *Phys. Rev. B* **1998**, *58*, 14922.
(34) Mohn, P.; Persson, C.; Blaha, P.; Schwarz, K.; Novak, P.; Eschrig, H. *Phys. Rev. Lett.* **2001**, *87*, 196401.
(35) Smirnov, A. V.; Shelton, W. A.; Johnson, D. D. *Phys. Rev. B* **2005**, *71*, 064408.
(36) Freeman, A. J.; Xu, J. H.; Hong, T.; Lin, W. *NATO ASI Series, Series E: Appl. Sci.* **1992**, *213*, 1.
(37) Niculescu, V. A.; Burch, T. J.; Budnick, J. I. *J. Magn. Magn. Mater.* **1983**, *39*, 223.
(38) Villars, P.; Calvert, L. D. *Pearson's Handbook of Crystallographic Data for Intermetallic Phases*; American Society for Metals: Materials Park, OH, 1985.
(39) Rausch, J. B.; Kayser, F. X. *J. Appl. Phys.* **1977**, *48*, 487.
(40) Arya, A.; Carter, E. A. *J. Chem. Phys.* **2003**, *118*, 8982.
(41) Hammer, L.; Graupner, H.; Blum, V.; Heinz, K.; Ownby, G. W.; Zehner, D. M. *Surf. Sci.* **1998**, *413*, 69.
(42) Heinz, K.; Hammer, L. *J. Phys.: Condens. Matter* **1999**, *11*, 8377.
(43) Blum, V.; Hammer, L.; Meier, W.; Heinz, K. *Surf. Sci.* **2001**, *488*, 219.
(44) Blum, V.; Hammer, L.; Meier, W.; Heinz, K.; Schmid, M.; Lundgren, E.; Varga, P. *Surf. Sci.* **2001**, *474*, 81.
(45) Meier, W.; Blum, V.; Hammer, L.; Heinz, K. *J. Phys.: Condens. Matter* **2001**, *13*, 1781.
(46) Starke, U.; Meier, W.; Rath, C.; Schardt, J.; Weiss, W.; Heinz, K. *Surf. Sci.* **1997**, *377*, 539.
(47) Starke, U.; Schardt, J.; Weiss, W.; Meier, W.; Polop, C.; de Andres, P. L.; Heinz, K. *Europhys. Lett.* **2001**, *56*, 822.
(48) Hammer, L.; Meier, W.; Blum, V.; Heinz, K. *J. Phys.: Condens. Matter* **2002**, *14*, 4145.
(49) Kizilkaya, O.; Hite, D. A.; Zehner, D. M.; Sprunger, P. T. *J. Phys.: Condens. Matter* **2004**, *16*, 5395.
(50) Wang, C. P.; Jona, F.; Gleason, N. R.; Strongin, D. R.; Marcus, P. M. *Surf. Sci.* **1993**, *298*, 114.
(51) den Boer, M. L.; Einstein, T. L.; Elam, W. T.; Park, R. L.; Roelofs, L. D. *Phys. Rev. Lett.* **1980**, *44*, 496.
(52) Duarte, H. A.; Salahub, D. R. *J. Chem. Phys.* **1998**, *108*, 743.
(53) Kittel, C. *Introduction to Solid State Physics*, 6th ed.; Wiley: New York, 1996.
(54) Jiang, D. E.; Carter, E. A. *Phys. Rev. B* **2004**, *70*, 064102.
(55) Merrill, P. B.; Madix, R. J. *Surf. Sci.* **1996**, *347*, 249.
(56) Stumpf, R. *Phys. Rev. Lett.* **1997**, *78*, 4454.
(57) Somorjai, G. A. *Introduction to Surface Chemistry and Catalysis*; Wiley: New York, 1994.
(58) Lide, D. R. *Handbook of Chemistry and Physics*, 77th ed.; CRC Press: Boca Raton, FL, 1996.
(59) Moon, D. W.; Bernasek, S. L.; Dwyer, D. J.; Gland, J. L. *J. Am. Chem. Soc.* **1985**, *107*, 4363.
(60) Paul, J.; Hoffmann, F. M. *Chem. Phys. Lett.* **1986**, *130*, 160.
(61) Jiang, D. E.; Carter, E. A. *J. Am. Chem. Soc.* **2005**, submitted.
(62) Busse, H.; Eltester, B.; Kandler, J.; Castro, G. R.; Wandelt, K. *Surf. Sci.* **1995**, *333*, 685.
(63) Bu, Y.; Lin, M. C. *Surf. Sci.* **1993**, *298*, 94.
(64) Young, R. Y.; Brown, K. A.; Ho, W. *Surf. Sci.* **1995**, *336*, 85.
(65) Hu, D. Q.; Ho, W.; Chen, X. J.; Wang, S.; Goddard, W. A. *Phys. Rev. Lett.* **1997**, *78*, 1178.
(66) Nørskov, J. K.; Bligaard, T.; Logadottir, A.; Bahn, S.; Hansen, L. B.; Bollinger, M.; Bengaard, H.; Hammer, B.; Sljivancanin, Z.; Mavrikakis, M.; Xu, Y.; Dahl, S.; Jacobsen, C. J. H. *J. Catal.* **2002**, *209*, 275.
(67) Greeley, J.; Nørskov, J. K.; Mavrikakis, M. *Annu. Rev. Phys. Chem.* **2002**, *53*, 319.
(68) Benziger, J.; Madix, R. J. *Surf. Sci.* **1980**, *94*, 119.
(69) Sorescu, D. C.; Thompson, D. L.; Hurley, M. M.; Chabalowski, C. F. *Phys. Rev. B* **2002**, *66*, 035416.

(70) Bromfield, T. C.; Ferre, D. C.; Niemantsverdriet, J. W. *ChemPhysChem* **2005**, *6*, 254.
(71) Windham, R. G.; Koel, B. E.; Paffett, M. T. *Langmuir* **1988**, *4*, 1113.
(72) Young, D. J.; Smeltzer, W. W. *J. Electrochem. Soc.* **1976**, *123*, 229.
(73) Lauretta, D. S.; Kremser, D. T.; Fegley, B., Jr. *ICARUS* **1996**, *122*, 288.
(74) Schneider, A.; Viefhaus, H.; Inden, G.; Grabke, H. J.; Muller-Lorenz, E. M. *Mater. Corros.* **1998**, *49*, 336.
(75) Schneider, A.; Grabke, H. J. *Mater. Corros.* **2003**, *54*, 793.
(76) Gonzalez, L.; Miranda, R.; Ferrer, S. *Surf. Sci.* **1982**, *119*, 61.